Inorganic Chemistry

Article

Forum

Mononuclear Lanthanide Single Molecule Magnets Based on the Polyoxometalates [Ln(W$_5$O$_{18}$)$_2$]$^{9-}$ and [Ln(β_2-SiW$_{11}$O$_{39}$)$_2$]$^{13-}$ (Ln^{III} = Tb, Dy, Ho, Er, Tm, and Yb)

Murad A. AlDamen,[†] Salvador Cardona-Serra,[†] Juan M. Clemente-Juan,[†,‡] Eugenio Coronado,*,[†] Alejandro Gaita-Ariño,[†,§] Carlos Martí-Gastaldo,[†] Fernando Luis,[||] and Oscar Montero[||]

Instituto de Ciencia Molecular, Universidad de Valencia, Polígono la Coma s/n, 46980 Paterna, Spain, Department of Physics and Astronomy, University of British Columbia, 6224 Agricultural Road, Vancouver, British Columbia V6T 1Z1, Canada, Instituto de Ciencia de Materiales de Aragón, CSIC, Universidad de Zaragoza, Plaza San Francisco s/n, 50009 Zaragoza, Spain, and Fundación General Universidad de Valencia (FGUV), Plaça del Patriarca, 46002 Valencia, Spain

The first two families of polyoxometalate-based single-molecule magnets (SMMs) are reported here. Compounds of the general formula [Ln(W$_5$O$_{18}$)$_2$]$^{9-}$ (Ln^{III} = Tb, Dy, Ho, and Er) and [Ln(SiW$_{11}$O$_{39}$)$_2$]$^{13-}$ (Ln^{III} = Tb, Dy, Ho, Er, Tm, and Yb) have been magnetically characterized with static and dynamic measurements. Slow relaxation of the magnetization, typically associated with SMM-like behavior, was observed for [Ln(W$_5$O$_{18}$)$_2$]$^{9-}$ (Ln^{III} = Ho and Er) and [Ln(SiW$_{11}$O$_{39}$)$_2$]$^{13-}$ (Ln^{III} = Dy, Ho, Er, and Yb). Among them, only the [Er(W$_5$O$_{18}$)$_2$]$^{9-}$ derivative exhibited such a behavior above 2 K with an energy barrier for the reversal of the magnetization of 55 K. For a deep understanding of the appearance of slow relaxation of the magnetization in these types of mononuclear complexes, the ligand-field parameters and the splitting of the *J* ground-state multiplet of the lanthanide ions have been also estimated.

Introduction

Most single-molecule magnets (SMMs) are polynuclear complexes formed by magnetic clusters of exchange-coupled metal ions with high-spin ground states and predominant uniaxial anisotropy.[1,2] The possibility of constructing SMMs using a single lanthanide ion has been recently demonstrated by Ishikawa in phthalocyaninatolanthanide complexes with a "double-decker" structure, [LnPc$_2$]$^-$.[3] In these complexes, a trivalent lanthanide ion, Ln^{III}, is encapsulated by two π-conjugated planar ligands (Pc = phthalocyanine dianion;

Ln^{III} = Tb, Dy, Ho, Er, Tm, and Yb). These ligands present four coordinating pyrrole nitrogen atoms in a square-planar symmetry. When two tetradentate ligands encapsulate the Ln^{III} ion, each moiety is twisted ca. 45° with respect to the other, generating a D_{4d} ligand-field (LF) symmetry around the lanthanide.

---

* To whom correspondence should be addressed. E-mail: eugenio.coronado@uv.es. Tel: +34-963544415. Fax: +34-963543273.
† Universidad de Valencia.
‡ Fundación General Universidad de Valencia.
§ University of British Columbia.
|| Universidad de Zaragoza.

(1) (a) Sessoli, R.; Gatteschi, D.; Caneschi, A.; Novak, M. A. *Nature* **1993**, *365*, 141–143. (b) Gatteschi, D.; Sessoli, R. *Angew. Chem., Int. Ed.* **2003**, *42*, 268–297. (c) Gatteschi, D.; Sessoli, R.; Villain, J. *Molecular Nanomagnets*; Oxford University Press: Oxford, U.K., 2006.

(2) For examples, see: (a) Mallah, T.; Auberger, C.; Verdaguer, M.; Veillet, P. *J. Chem. Soc., Chem. Commun.* **1995**, *61*, 62. (b) Castro, S. L.; Sun, Z. M.; Grant, C. M.; Bollinger, J. C.; Hendrickson, D. N.; Christou, G. *J. Am. Chem. Soc.* **1998**, *120*, 2365–2375. (c) Barra, A. L.; Caneschi, A.; Cornia, A.; de Biani, F. F.; Gatteschi, D.; Sangregorio, C.; Sessoli, R.; Sorace, L. *J. Am. Chem. Soc.* **1999**, *121*, 5302–5310. (d) Barra, A. L.; Caneschi, A.; Gatteschi, D.; Goldberg, D. P.; Sessoli, R. *J. Solid State Chem.* **1999**, *145*, 484–487. (e) Yoo, J.; Brechin, E. K.; Yamaguchi, A.; Nakano, M.; Huffman, J. C.; Maniero, A. L.; Brunel, L. C.; Awaga, K.; Ishimoto, H.; Christou, G.; Hendrickson, D. N. *Inorg. Chem.* **2000**, *39*, 3615–3623. (f) Sokol, J. J.; Hee, A. G.; Long, J. R. *J. Am. Chem. Soc.* **2002**, *124*, 7656–7657. (g) Berlinguette, C. P.; Vaughn, D.; Canada-Vilalta, C.; Galan-Mascaros, J. R.; Dunbar, K. R. *Angew. Chem., Int. Ed.* **2003**, *42*, 1523–1526.

(3) Ishikawa, N.; Sugita, M.; Ishikawa, T.; Koshihara, S.; Kaizu, Y. *J. Am. Chem. Soc.* **2003**, *125*, 8694–8695.

In this class of single-atom nanomagnets, the magnetic anisotropy required for observing slow relaxation of the magnetization arises from the splitting of the J ground state of the Ln^{III} ion when it is submitted to a LF. For certain LF symmetries, such a splitting can stabilize sublevels with a large $|M_J|$ value, thus achieving an easy axis of the magnetization.[4] Some years ago, Ishikawa developed a convenient procedure to determine the LF parameters and the sublevel structure of the phthalocyaninatolanthanide complexes.[5] The approach involves a simultaneous least-squares fit of the magnetic susceptibility data and ^{1}H NMR paramagnetic shifts for the whole set of compounds. The best set of LF parameters gave large positive values for $A_0^2 r^2$ and large negative values for $A_0^4 r^4$ in the phthalocyaninato complexes.[6] Under these conditions, the ground-state sublevels for Tb, Dy, and Ho turned out to be doublets with large $|M_J|$ values, for Tb reaching the maximum value ($M_J = \pm 6$). Furthermore, in this case, the ground-state sublevel is well isolated from the first excited one (by more than 400 cm^{-1}). The ground-state sublevels of the other lanthanides turned out to be doublets with low $|M_J|$ values. For example, in the Er case, this sublevel corresponds to that with the minimum $|M_J|$ value ($\pm^1/_2$). Accordingly, from the six members of the family, only Tb and Dy derivatives exhibited SMM behavior, with frequency-dependent out-of-phase alternating current (ac) susceptibility peaks at 40 and 10 K, respectively. In these nanomagnets, the relaxation processes were associated with a thermally activated Orbach process involving excited sublevels of the ground J multiplet. Resonant quantum tunneling of the magnetization, which is a characteristic feature of SMMs, was also observed in the Ho derivative.[7]

Still, few studies on the mononuclear lanthanide-based complexes exhibiting SMM behavior, apart from the phthalocyaninatolanthanide complexes, have been reported. In this context, we have shown in a previous communication that polyoxometalates (POMs) encapsulating lanthanides with coordination geometries similar to those of bis(phthalocyaninato)lanthanide complexes can also exhibit SMM behavior.[8] This was firstly demonstrated in the sodium salt of the polyanion $[Er(W_5O_{18})_2]^{9-}$. In the present work, we report a detailed magnetostructural characterization for the whole family $[Ln(W_5O_{18})_2]^{9-}$ (Ln^{III} = Tb, Dy, Ho, and Er) and extend this study to the series $[Ln(SiW_{11}O_{39})_2]^{13-}$ (Ln^{III} = Tb, Dy, Ho, Er, Tm, and Yb).

Experimental Section

Synthesis. All reagents and solvents were of commercially available grade and used without any previous purification. $LnCl_3 \cdot 6H_2O$ and $Er_2(CO_3)_2 \cdot xH_2O$ are highly hygroscopic compounds; for that reason,

they were stored in desiccators. The monolacunary Keggin precursor, $K_8[(\beta_2\text{-}SiW_{11}O_{39}) \cdot 14H_2O$, was prepared according to a previously described procedure[9] and identified by electron probe microanalysis (EPMA) and FT-IR techniques (SI 1 and SI 2 in the Supporting Information).

$Na_9[Tb(W_5O_{18})_2] \cdot xH_2O$ (**1**) was prepared following a previously described procedure[10] with slight modifications. A total of 8.3 g (25 mmol) of $Na_2WO_4 \cdot 2H_2O$ was dissolved in 20 mL of water. The resulting solution was adjusted to pH 7.4−7.5 with acetic acid. Subsequently, an aqueous solution (2 mL) containing 0.921 (2.5 mmol) of $TbCl_3 \cdot 6H_2O$ was added dropwise to the above-mentioned solution under continuous stirring and heated up to 85 °C. Crude crystals were isolated when this solution was left to stand at room temperature. FT-IR data in cm^{-1}: 935 (s), 845 (s), 798 (m), 706 (m), 586 (w), 545 (m), 490 (w).

$Na_9[Dy(W_5O_{18})_2] \cdot xH_2O$ (**2**) was prepared as previously described for **1** but using 0.930 g (2.5 mmol) of $DyCl_3 \cdot 6H_2O$. FT-IR data in cm^{-1}: 933 (s), 847 (s), 804 (m), 705 (m), 584 (w), 549 (m), 490 (w).

$Na_9[Ho(W_5O_{18})_2] \cdot xH_2O$ (**3**) was prepared as previously described for **1** but using 0.940 g (2.5 mmol) of $HoCl_3 \cdot 6H_2O$. FT-IR data in cm^{-1}: 933 (s), 847 (s), 804 (m), 708 (m), 596 (w), 546 (m), 422 (w).

$Na_9[Er(W_5O_{18})_2] \cdot xH_2O$ (**4**) was prepared following a previously described method.[11] In a first stage, $Er_2(CO_3)_2 \cdot xH_2O$ (2.180 g, 3.8 mmol) was dissolved in 30 mL of HCl (0.1 M) and heated at 80 °C for 30 min, giving rise to a colorless solution (A). Simultaneously, $Na_2WO_4 \cdot 2H_2O$ (50 g, 152 mmol) was dissolved in distilled water (100 mL) with continuous stirring; the pH was adjusted to 7.2 with acetic anhydride, and the resulting solution (B) was heated to 90 °C. Then, A was dropwise added to the hot stirred wolframate solution (B). After being vigorously stirred for 1 h, the mixture was filtered rapidly and left to evaporate at room temperature. A total of 3 weeks later needle-shaped pale-pink crystals of **4**, suitable for single-crystal X-ray diffraction, were obtained. FT-IR data for **1** in cm^{-1}: 935 (s), 845 (s), 798 (m), 706 (m), 586 (w), 545 (m), 490 (w).

$K_{13}[Tb(\beta_2\text{-}SiW_{11}O_{39})_2] \cdot xH_2O$ (**5**) was prepared by following a previously described method.[12] A total of 0.5 g (0.15 mmol) of $K_8[\beta_2\text{-}SiW_{11}O_{39}] \cdot 14H_2O$ and 0.0319 g (0.085 mmol) of $TbCl_3 \cdot 6H_2O$ were added to 20 mL of 1 M KCl. The resulting mixture was adjusted to pH 4.4−5.0 by the dropwise addition of 0.1 M HCl. Afterward, the solution was mechanically stirred at 50 °C for 30 min and allowed to stand at room temperature. Rapid filtration, followed by slow evaporation in an open container at room temperature, yielded crystals suitable for X-ray diffraction, after 3 days. FT-IR data in cm^{-1}: 1003 (m), 957 (m), 910 (s), 872 (s), 837 (m), 789 (s), 725 (s).

$K_{13}[Dy(\beta_2\text{-}SiW_{11}O_{39})_2] \cdot xH_2O$ (**6**) was prepared as previously described for **5** but using 0.032 g (0,085 mmol) of $DyCl_3 \cdot 6H_2O$. FT-IR data in cm^{-1}: 1005 (m), 953 (m), 910 (s), 877 (s), 837 (m), 793 (s), 727 (s).

$K_{13}[Ho(\beta_2\text{-}SiW_{11}O_{39})_2] \cdot xH_2O$ (**7**) was prepared as previously described for **5** but using 0.032 g (0,085 mmol) of $HoCl_3 \cdot 6H_2O$. FT-IR data in cm^{-1}: 1008 (m), 954 (m), 915 (s), 877 (s), 838 (m), 794 (s), 720 (s);.

(4) Ishikawa, N.; Sugita, M.; Ishikawa, T.; Koshihara, S.; Kaizu, Y. *J. Phys. Chem. B* **2004**, *108*, 11265–11271.

(5) Ishikawa, N.; Iino, T.; Kaizu, Y. *J. Phys. Chem. A* **2002**, *106*, 9543. Ishikawa, N.; Iino, T.; Kaizu, Y. *J. Am. Chem. Soc.* **2002**, *124*, 11440.

(6) Ishikawa, N.; Sugita, M.; Okubo, T.; Takana, N.; Iino, T.; Kaizu, Y. *Inorg. Chem.* **2003**, *42*, 2440.

(7) (a) Ishikawa, N.; Sugita, M.; Wernsdorfer, W. *Angew. Chem., Int. Ed.* **2005**, *22*, 2931. (b) Ishikawa, N.; Sugita, M.; Wernsdorfer, W. *J. Am. Chem. Soc.* **2005**, *127*, 3650.

(8) Aldamen, M.; Clemente-Juan, J. M.; Coronado, E.; Martí-Gastaldo, C.; Gaita-Ariño, A. *J. Am. Chem. Soc.* **2008**, *130*, 8874–8875.

(9) Tézé, A.; Hervé, G. *Inorg. Chem.* **1990**, *27*, 88.

(10) Ozeki, T.; Yamase, T. *Acta Crystallogr.* **1994**, *C50*, 327.

(11) Shiozaki, R.; Inagaki, A.; Nishino, A.; Nishio, E.; Maekawa, M.; Kominami, H.; Kera, Y. *J. Alloys Compd.* **1996**, *234*, 193.

(12) Bassil, B. S.; Dickman, M. H.; Von der Kammer, B.; Kortz, U. *Inorg. Chem.* **2007**, *46*, 2452.

Table 1. Summary of the Structural Data of **4**[a]

formula	$Na_9ErW_{10}O_{71}H_{68}$
mol wt	3348.6
T [K]	173(2)
λ [Å]	0.710 73
cryst syst	triclinic
space group	$P\bar{1}$
a [Å]	12.744(3)
b [Å]	13.071(3)
c [Å]	20.470(4)
α [deg]	82.89(3)
β [deg]	74.53(3)
γ [deg]	88.80(3)
V [Å³]	3260.8(11)
Z	2
ρ_{calcd} [g cm⁻³]	3.411
2θ limit [deg]	2.18−30.09
GOF	0.984
R1	0.0714
R2	0.1905

[a] R1 $= \sum(F_o - F_c)/\sum(F_o)$. R2 $= [\sum[w(F_o^2 - F_c^2)^2]/\sum[w(F_o^2)^2]]^{1/2}$; $w = 1/[\sigma^2(F_o^2) + (0.0343P)^2 + 2.4502P]$; $P = (F_o^2 + 2F_c^2)/3$.

$K_{13}[Er(\beta_2\text{-}SiW_{11}O_{39})_2] \cdot xH_2O$ (**8**) was prepared as previously described for **5** but using 0.0326 g (0,085 mmol) of $ErCl_3 \cdot 6H_2O$. FT-IR data in cm⁻¹: 1008 (m), 958 (m), 915 (s), 878 (s), 836 (m), 790 (s), 724 (s).

$K_{13}[Tm(\beta_2\text{-}SiW_{11}O_{39})_2] \cdot xH_2O$ (**9**) was prepared as previously described for **5** but using 0.0326 g (0,085 mmol) of $TmCl_3 \cdot 6H_2O$. FT-IR data in cm⁻¹: 1009 (m), 957 (m), 912 (s), 876 (s), 837 (m), 789 (s), 723 (s).

$K_{13}[Yb(\beta_2\text{-}SiW_{11}O_{39})_2] \cdot xH_2O$ (**10**) was prepared as previously described for **5** but using 0.039 g (0,085 mmol) of $YbCl_3 \cdot 6H_2O$. FT-IR data in cm⁻¹: 1007 (m), 957 (m), 914 (s), 879 (s), 837 (m), 787 (s), 723 (s).

X-ray Data Collection. Crystals were collected by hand, fixed on a 200 μm MicroMount,[13] and mounted on a Nonius-Kappa CCD single-crystal diffractometer equipped with graphite-monochromated Mo Kα radiation ($\lambda = 0.710\ 73$ Å) at 293(2) or 173(2) K. Data collection was performed by using the program *Collect*.[14] Data reduction and cell refinement were performed with the programs *Denzo* and *Scalepack*.[15] The crystal structure was solved by direct methods using the program *SIR97*,[16] followed by Fourier synthesis, and refined on F^2 with *SHELXL-97*.[17] Anisotropic least-squares refinement of all non-disordered heavy atoms (Ln, W, Si, Na, and O) was performed. All crystallographic plots were obtained using the *CrystalMaker* program.[18] Tables 1 and 3 summarize the crystal data collection and refinement parameters.

ICSD 419267, 419778, and 419779 files contain the supplementary crystallographic data for this paper. They can be obtained free

(13) Thorne, R. E.; Stum, Z.; Kmetko, J.; O'Neill, K.; Gillilan, R. *J. Appl. Crystallogr.* **2003**, *36*, 1455–1460.
(14) Collect, Nonius BV, 1997−2000.
(15) Otwinowsky, Z.; Minor W. In *Processing of X-ray diffraction data collected in oscillation mode*; Carter, C. W., Jr., Sweet, R. M., Eds.; Academic Press: New York, 1997.
(16) Altomare, A.; Burla, M. C.; Camalli, M.; Cascarano, G. L.; Giacovazzo, C.; Guagliardi, A.; Moliterni, A. G. G.; Polidori, A.; Spagna, G. *J. Appl. Crystallogr.* **1999**, *32*, 115–119.
(17) Sheldrick, G. M. *SHELXL-97*; University of Göttingen: Göttingen, Germany, 1997.
(18) *CrystalMaker Software*; CrystalMaker Software Limited: Oxfordshire, U.K., 2006.
(19) (a) Ostendorp, G.; Werner, J. P.; Homborg, H. *Acta Crystallogr., Sect. C: Cryst. Struct.* **1995**, *51*, 1125–1128. (b) Koike, N.; Uekusa, H.; Ohashi, Y.; Harnoode, C.; Kitamura, F.; Ohsaka, T.; Tokuda, K. *Inorg. Chem.* **1996**, *35*, 5798–5804.
(20) Stevens, K. W. H. *Proc. Phys. Soc. A* **1952**, *65*, 209–215.
(21) (a) Orbach, R. *Proc. Phys. Soc. A* **1961**, *264*, 458–484. (b) Rudowicz, C. *J. Phys. C: Solid State Phys.* **1985**, *18*, 1415–1430.
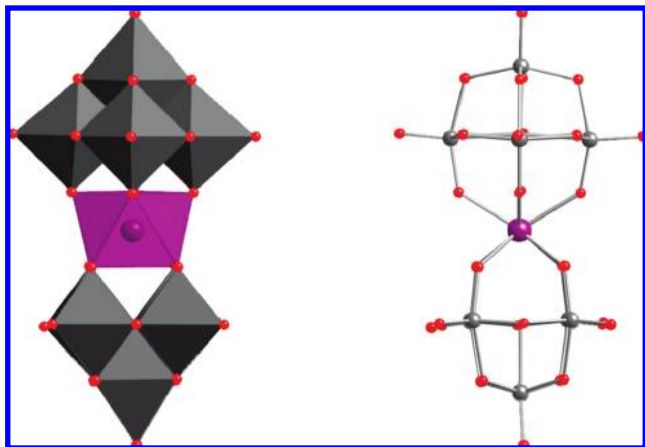
Table 2. Structural Parameters Concerning the Lanthanide Coordination Sphere in the Series $[LnW_{10}O_{36}]^{9-}$

$[Ln^{III}W_{10}O_{36}]^{9-}$	countercation	d_{pp}[b] [Å]	d_{in}[a] [Å]	φ[c] [deg]	ref
Pr	3 K⁺, 4 Na⁺, 2 H⁺	2.667	2.955	41.4	27
Nd	3 K⁺, 4 Na⁺, 2 H⁺	2.615	2.948	43.2	27
Sm	6 Na⁺, 3 H⁺	2.575	2.921	46.9	28
Sm	3 K⁺, 4 Na⁺, 2 H⁺	2.695	2.926	46.9	27
Eu	9 Na⁺	2.356	2.608	46.7	29
Eu	4 Sr²⁺, 1 Na⁺	2.556	2.878	41.2	30
Gd	3 K⁺, 4 Na⁺, 2 H⁺	2.635	2.892	43	31
Gd	8 Na⁺, 1 H⁺	2.539	2.898	39.1	32
Dy	9 Na⁺	2.496	2.876	44.0	33
Dy	3 K⁺, 4 Na⁺, 2 H⁺	2.551	2.864	43.1	27
Er	9 Na⁺	2.469	2.856	44.5	this work

[a] d_{in} is the average O−O distance within the oxygen-based square planes. [b] The d_{pp} parameter defines the average distance between the two oxygen-based square planes. [c] φ is defined as the relative orientation between the two squares defined by the coordinating oxygen atoms (see the text).

Table 3. Summary of the Structural Data of **8** and **9**[a]

formula	$K_{13}ErW_{22}O_{103}H_{50}$	$K_{13}TmW_{22}O_{103}H_{50}$
mol wt	6474.5	6476.2
T [K]	173(2)	293(2)
λ [Å]	0.710 73	0.710 73
cryst syst	monoclinic	monoclinic
space group	$P21/c$	$P21/c$
a [Å]	20.208(4)	20.196(7)
b [Å]	20.535(3)	20.522(7)
c [Å]	27.294(5)	27.232(8)
α [deg]	90	90
β [deg]	113.805(7)	113.791(1)
γ [deg]	90	90
V [Å³]	10362.6(2)	10327.5(4)
Z	4	4
ρ_{calcd} [g cm⁻³]	4.09	3.80
2θ limit [deg]	2.51−27.48	1.46−30.02
GOF	1.028	1.030
R1	0.0817	0.0948
R2	0.2084	0.2889

[a] R1 $= \sum(F_o - F_c)/\sum(F_o)$. R2 $= [\sum[w(F_o^2 - F_c^2)^2]/\sum[w(F_o^2)^2]]^{1/2}$; $w = 1/[\sigma^2(F_o^2) + (0.0343P)^2 + 2.4502P]$; $P = (F_o^2 + 2F_c^2)/3$.

of charge via http://www.fiz-karlsruhe.de/obtaining_crystal_structure_data.html or from the Inorganic Crystal Structure Database (ICSD, FIZ Kalsruhe, Hermann-von-Helmholtz-Platz 1, Eggenstein-Leopoldshafen, 76344, Germany; phone (+49) 7247-808-555, fax (+49) 7247-808-259).

Physical Measurements. The metallic composition of bulk samples was determined by EPMA performed in a Philips SEM XL30 equipped with an EDAX DX-4 microsonde. IR spectra were recorded on a FT-IR Nicolet 5700 spectrometer in the 4000−400 cm⁻¹ range using powdered, hand-collected crystal samples in KBr pellets. Magnetic susceptibility measurements were performed on previously ground, hand-collected crystals with a Quantum Design MPMS-XL-5 magnetometer equipped with a SQUID sensor and a Quantum Design model PPMS-9. The susceptibility data were corrected from the diamagnetic contributions as deduced by using Pascal's constant tables. Direct current (dc) data were collected in the range 2−300 K with an applied field of 1000 G. Alternate current (ac) data were collected in the range 2−12 K with an applied alternating field of 3.95 G at different frequencies in the range 1−10000 Hz.

Results and Discussion

Structural Characterization. Here we report the magnetostructural study of two series of mononuclear lanthanide-based complexes obtained by encapsulation of the lanthanide metal by two monolacunary POM anions acting

Figure 1. Polyhedral (left) and ball-and-stick (right) representations of the $[Ln(W_5O_{18})_2]^{9-}$ cluster (oxygen, red; tungsten, gray; lanthanide, purple). This structure can be considered representative of the whole set of compounds: Ln^{III} = Tb (**1**), Dy (**2**), Ho (**3**), and Er (**4**).
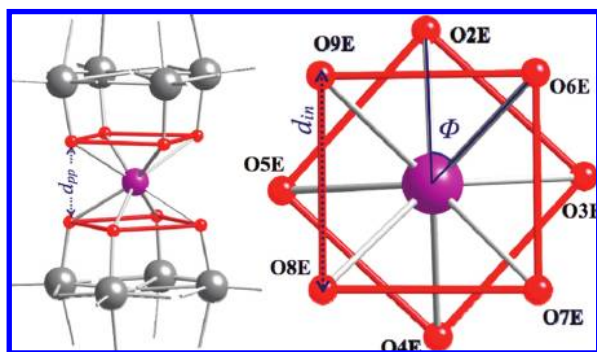

Figure 2. Perspective showing the square-antiprismatic coordination of the central Ln^{3+} ion and the d_{pp} parameter in $[Ln(W_5O_{18})_2]^{9-}$ (left). Perspective showing the d_{in} and ϕ structural features (right).

as tetradentate ligands. When the monolacunary $[W_5O_{18}]^{6-}$ anion derived from the Lindqvist anion $[W_6O_{19}]^{2-}$ is used, one obtains the series $[Ln(W_5O_{18})_2]^{9-}$ [Ln^{III} = Tb (**1**), Dy (**2**), Ho (**3**), and Er (**4**); see Figure 1). On the other hand, when the monolacunary $[\beta_2\text{-}SiW_{11}O_{39}]^{8-}$ anion derived from the Keggin anion $[SiW_{12}O_{40}]^{4-}$ is used, one obtains the series $[Ln(\beta_2\text{-}SiW_{11}O_{39})_2]^{13-}$ [Ln^{III} = Tb (**5**), Dy (**6**), Ho (**7**), Er (**8**), Tm (**9**), and Yb (**10**); Figure 3). Notice that the synthesis and structures of the first series were already reported for the derivatives Ln^{III} = Pr,[27] Nd,[27] Sm,[27,28] Eu,[29,30] Gd,[31,32] Tb,[27] and Dy.[27,33] Among them,

(22) (a) Fedotov, M. A.; Samokhvalova, E. P.; Kazansky, L. P. *Polyhedron* **1996**, *15*, 3341–3351. (b) Shiozaki, R.; Inagaki, A.; Nishino, A.; Nishio, E.; Maekawa, M.; Kominami, H.; Kera, Y. *J. Alloys Compd.* **1996**, *234*, 193–198.

(23) (a) Cole, K. S.; Cole, R. H. *J. Chem. Phys.* **1941**, *9*, 341–351. (b) Dekker, C.; Arts, A. F. M.; Dewijn, H. W.; Vanduyneveldt, A. J.; Mydosh, J. A. *Phys. Rev. B* **1989**, *40*, 11243–11251.

(24) (a) Clemente-Juan, J. M.; Coronado, E. *Chem. Rev.* **1999**, *193*, 361–394. (b) Coronado, E.; Gómez-García, C. J. *Chem. Rev.* **1998**, *98*, 273–296. (c) Müller, A.; Peters, F.; Pope, M. T.; Gatteschi, D. *Chem. Rev.* **1998**, *98*, 239–272. (d) Calzado, C. J.; Clemente-Juan, J. M.; Coronado, E.; Gaita-Arino, A.; Suaud, N. *Inorg. Chem.* **2008**, *47*, 5889–5901, and references cited therein. .

(25) (a) Lehmann, J.; Gaita-Arino, A.; Coronado, E.; Loss, D. *Nature Nanotechnol.* **2007**, *2*, 312–317. (b) Bertaina, S.; Gambarelli, S.; Mitra, T.; Tsukerblat, B.; Müller, A.; Barbara, B. *Nature* **2008**, *453*, 203–206.

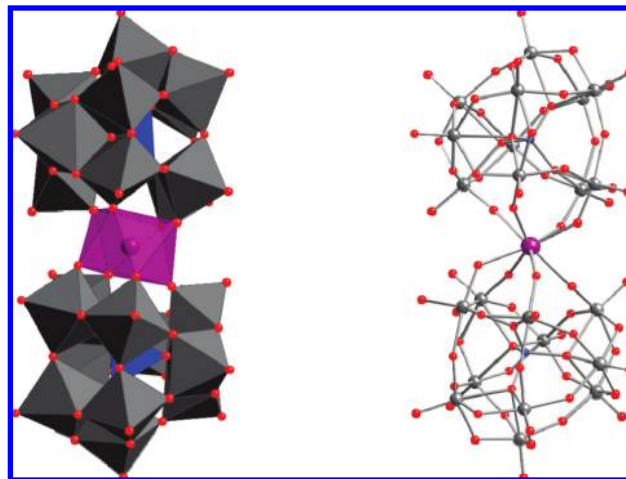**Figure 3.** Polyhedral (left) and ball-and-stick (right) representations of the $[Ln(\beta_2\text{-}SiW_{11}O_{39})_2]^{13-}$ cluster (oxygen, red; silicon, blue; tungsten, gray; lanthanide, purple). This structure can be considered representative of the whole set of compounds: Ln^{III} = Tb (**5**), Dy (**6**), Ho (**7**), Er (**8**), Tm (**9**), and Yb (**10**).

only the Eu and Dycompounds were isolated as sodium salts (see Table 2). Concerning the second series, the synthesis and structures of their potassium salts were first reported by Bassil et al. for the derivatives Ln^{III} = La, Ce, Sm, Eu, Gd, Tb, Yb, and Lu.[12] The compounds described in this work have been isolated as hydrated eneasodium (**1–4**) and tridecapotassium salts (**5–10**), respectively, and characterized by FT-IR and EPMA. Although important efforts have been devoted to obtain the decawolframelanthanoatothulim and -ytterbium derivatives, we could not isolate them as pure phases. Because the SMM behavior observed in mononuclear lanthanide-based POMs is strongly dependent on the exact coordination geometry around the metal, important attention has been devoted to the analysis of their crystal structures.

$[Ln(W_5O_{18})_2]^{9-}$ Series [Ln^{III} = Tb (1), Dy (2), Ho (3), and Er (4)]. Considering that all the synthesized compounds are isostructural, we have only determined the crystal structure of the Er complex. It is formed by two anionic $[W_5O_{18}]^{6-}$ moieties sandwiching the central lanthanide ion (Figures 1 and 2). The anionic clusters are surrounded by sodium cations that are octahedrally coordinated by oxygen atoms, with Na–O distances in the range 2.235–2.684 Å (average 2.429 Å), apart from Na6, which exhibits square-pyramidal coordination, with Na–O distances in the range 2.280–2.362 Å (average 2.326 Å). These NaO_n (n = 5 and 6) clusters are connected by edge- and corner-sharing linkages. These hydrated Na^+ cations interact with the highly charged $[Er(W_5O_{18})_2]^{9-}$ anions for electroneutrality, thus introducing a large number of water molecules in the lattice, as has been previously observed in other sodium salts of decawolframolanthanoate. This fact, together with

(26) Ritchie, C.; Ferguson, A.; Nojiri, H.; Miras, H. N.; Song, Y. F.; Long, D. L.; Burkholder, E.; Murrie, M.; Kogerler, P.; Brechin, E. K.; Cronin, L. *Angew. Chem., Int. Ed.* **2008**, *47*, 5609–5612.

(27) Ozeki, T.; Yamase, T. *Acta Crystallogr.* **1994**, *B50*, 128.

(28) Ozeki, T.; Yamase, T. *Acta Crystallogr.* **1994**, *C50*, 327.

(29) Sugeta, M.; Yamase, T. *Bull. Chem. Soc. Jpn.* **1993**, *66*, 444.

(30) Ozeki, T.; Yamase, T.; Kosaka, M. *Acta Crystallogr.* **1993**, *C50*, 1849.

the presence of the bulky POM ligand $[W_5O_{18}]^{6-}$, results in good isolation of the anisotropic Ln^{3+} ions in the solid state (shortest Er−Er distance of 11.225 Å).

Regarding the lanthanide inner coordination sphere, the skew angle (ϕ) can be defined either as the rotation angle between the two rotating triads, each of them belonging to different $[W_5O_{18}]^{6-}$ moieties, or as the offset between the two squares defined by the mean planes through the coordinating oxygen atoms (O2E, O3E, O4E, O5E and O6E, O7E, O8E, O9E; Figure 2). In this particular case, each anionic moiety is twisted 44.2° with respect to the other. This angle is very close to that expected for an ideal D_{4d} symmetry ($\phi = 45°$). Therefore, the coordination site can be described as slightly distorted square-antiprismatic (Figure 2). Er−O distances also support this minor distortion because they range from 2.339(3) to 2.387(3) Å (average value 2.367(7) Å). This geometry corresponds to an approximate D_{4d} LF symmetry, which is also that exhibited by the series of "double-decker" phthalocyanine complexes. However, in this last case, the geometry around the Er^{3+} ion is more distorted with a skew angle of 41.4°. In addition, in the reported compound, the ratio between the interplanar distance $d_{pp} = 2.47(1)$ Å, calculated as the distance between the upper and lower planes containing the four oxygen atoms, and the average distance between the four neighboring oxygen atoms placed in each plane, $d_{in} = 2.86(5)$ Å, is indicative of a certain axial compression of the square antiprism built up by the 8-fold-coordinated Er^{3+} ion. This fact contrasts with the axial elongation exhibited by the "double-decker" phthalocyanine complexes.[19] Concerning the above-mentioned oxygen-based square planes, the φ angle can be defined as well. This parameter, estimated as the angle between the planes' normal vectors, is useful to check the distortion, if any, from perfect coplanarity between the coordinating planes. In the Er complex, φ was found to be 0°, thus confirming minimum deviation from the ideal D_{4d} symmetry.

All of these geometrical differences in the lanthanide coordination sites with respect to the phthalocyaninate complexes, although small, seem to be sufficient to completely change the magnetic relaxation properties of these lanthanide-based complexes.

$[Ln(\beta_2\text{-}SiW_{11}O_{39})_2]^{13-}$ [Ln^{III} = Tb (5), Dy (6), Ho (7), Er (8), Tm (9), and Yb (10)]. Taking into account that all the synthesized compounds were isostructural, crystal structures have only been determined for derivatives **8** and **9**. The identities of **5**−**10** were confirmed by FT-IR and EPMA. These dimeric polyanionic species are composed of a central Ln^{3+} encapsulated by two $(\beta_2\text{-}SiW_{11}O_{39})^{8-}$ units in a distorted square-antiprismatic coordination (pseudo-D_{4d} symmetry; Figure 3). The anionic POM moieties are surrounded by potassium cations for charge balance. Average K−O_W distances are found to be 2.837 and 2.812 Å for **8** and **9**, respectively. As previously indicated for the $[Ln(W_5O_{18})_2]^{9-}$ family, the large number of water molecules present in the crystalline lattice, together with the presence of the bulky POM ligands (β_2-
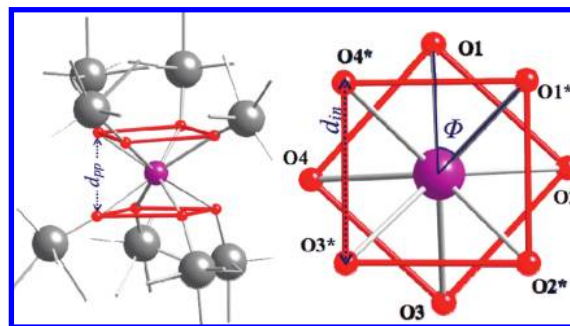

Figure 4. Perspective showing the square-antiprismatic coordination of the central Ln^{3+} ion and the d_{pp} parameter in $[Ln(\beta_2\text{-}SiW_{11}O_{39})_2]^{13-}$ (left). Perspective showing the d_{in} and ϕ structural features (right).

$SiW_{11}O_{39})^{8-}$, results in a good isolation of the anisotropic Ln^{3+} ions in the solid state (shortest Ln−Ln distance of 12.624 and 12.625 Å for Er and Tm derivatives). Ln^{3+} ions are connected to four oxygen atoms belonging to each monolacunary Keggin unit with Ln−O_W and Ln−W distances together with a O_W−Ln−O_W angle strongly affected by the size of the central atom (see Table 4). As expected, when the atomic number of the lanthanide is increased, a decrease of the average Ln−O_W and Ln−W distances is observed. This same effect has been observed for the other structural parameters such as the interplanar distance (d_{pp}), calculated as the distance between the upper and lower square planes containing the four oxygen atoms, and the average in-plane O_W−O_W distance (d_{in}), concerning the four neighboring oxygen atoms within each plane. Figure 5 shows the linear variation of these structural parameters with the Ln^{3+} ionic radius.

Focusing now on the coordination geometry of the metal complexes (Figure 4), one notices that the ratio between d_{pp} and d_{in} distances is indicative of the presence of a certain compression of the square antiprism, similar to what has been observed in the $[Ln(W_5O_{18})_2]^{9-}$ series. The other parameters (ϕ and φ angles), however, indicate larger distortions from the regular square-antiprismatic D_{4d} symmetry, as compared with the $[Ln(W_5O_{18})_2]^{9-}$ series. Indeed, the skew angle value (ϕ) has been found to be 47.5° and 48.0° for **8** and **9**, respectively. Besides, important deviations from coplanarity between the two coordinating planes have been observed with an average $\varphi = 2.8°$ value (see Table 4). These geometrical differences between the two families are general and should affect the LF parameters and, hence, the magnetic properties.

A final point that deserves to be mentioned concerns the chirality of the $(\beta_2\text{-}SiW_{11}O_{39})^{8-}$ anion. As previously described for the $[Ln(\beta_2\text{-}SiW_{11}O_{39})]^{13-}$ (Ln^{3+} = La, Ce, Sm, Eu, Gd, Tb, Yb, and Lu) series,[12] important attention must be paid to the absolute configuration of the molecular cluster resulting from the relative chirality of the two $(\beta_2\text{-}SiW_{11}O_{39})^{8-}$ moieties. Bassil et al. described these configurations as A, when the relative chirality of one lacunary Keggin unit with respect to the other was (R,R) or (S,S) and B for (S,R) and (R,S) relative configurations. Note that the A configuration is defined by a C_2 space group,

Table 4. Structural Parameters Concerning the Lanthanide Coordination Sphere in the Series $[Ln(\beta_2\text{-}SiW_{11}O_{39})]^{13-}$

$K_{13}[Ln(\beta_2\text{-}SiW_{11}O_{39})_2]$	Ln^{3+} radius[a] [Å]	$d(Ln-O_W)$ [Å]	$d(Ln-W)$ [Å]	d_{in}[b] [Å]	d_{pp}[c] [Å]	ϕ[d] [deg]	φ[e] [deg]	ref
La	1.061	2.49	4.050	2.964	2.681	39.9	4.1	12
Ce	1.034	2.46	4.028	2.937	2.653	40.8	3.1	12
Sm	0.964	2.41	3.989	2.872	2.583	41.3	2.9	12
Eu	0.950	2.40	3.982	2.863	2.566	44.4	0	12
Gd	0.938	2.40	3.975	2.863	2.566	42.9	2.8	12
Tb	0.923	2.37	3.961	2.833	2.458	44.6	2.8	12
Er	0.881	2.36	3.929	2.832	2.478	47.5	2.8	this work
Tm	0.869	2.60	3.919	2.850	2.477	48.0	2.8	this work
Yb	0.858	2.33	3.918	2.787	2.473	48.3	2.3	12
Lu	0.848	2.32	3.909	2.785	2.458	47.6	2.3	12

[a] Data were extracted from: Cotton, F. A.; Wilkinson, G. *Advanced Inorganic Chemistry*; Limusa: Madrid, Spain, 1998. [b] The d_{pp} parameter defines the average distance between the two oxygen-based square planes. [c] The d_{in} is the average O–O distance within the oxygen-based square planes. [d] ϕ is defined as the relative orientation between the two squares defined by the coordinating oxygen atoms (see the text). [e] φ is defined as the angle between the normal vectors of the oxygen-based square planes (see the text).
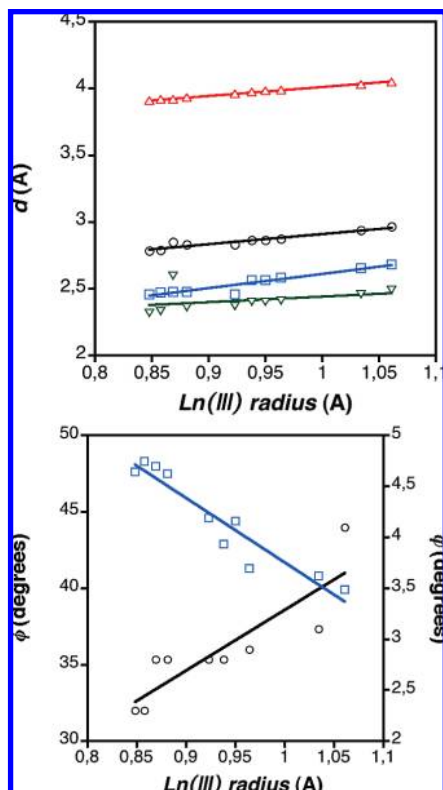

Figure 5. Dependence of the structural parameters concerning the lanthanides' coordination spheres with the Ln^{3+} ionic radius (see Table 4). Plotted data belong to the $[Ln(\beta_2\text{-}SiW_{11}O_{39})_2]^{9-}$ family and have been extracted from ref 12 and the present work. Solid thin lines represent the best linear fitting. (Top) $d(Ln-W)$: red triangles. d_{in}: black circles. d_{pp}: blue squares. $d(Ln-O)$: inverted green triangles. (Bottom) ϕ angle: blue squares. φ angle: black circles. The Eu derivative exhibited an anomalous φ value, and it has been omitted.

while the B configuration corresponds to C_1. For compounds **6–9**, only configuration B is observed. This fact is in good agreement with the previous observation that the chirality of the surrounding Keggin units depends on the size of the lanthanide. Indeed, these authors claimed that early lanthanide ions, attending to their bigger size, favor the A configuration, whereas when shifting to a smaller ionic radius, a gradual transition from the A to B configuration is favored. In this context, they observed that the $[Ln(\beta_2\text{-}SiW_{11}O_{39})_2]^{13-}$ systems encapsulating the
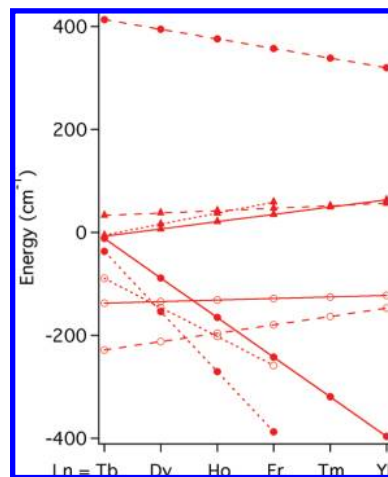
Figure 6. LF parameters $A_2^0\ r^2$ (●), $A_4^0\ r^4$ (○) and $A_6^0\ r^6$ (▲) of $Na_9[Ln(W_5O_{18})_2]\cdot xH_2O$ (dot lines), $K_{13}[Ln(\beta_2\text{-}SiW_{11}O_{39})_2]\cdot xH_2O$ (solid lines) and $[Pc_2Ln]TBA$ families (dashed lines).

smaller lanthanide ions, Yb and Lu, exhibited 100% of the B configuration.

dc Susceptibility Measurements. The magnetic properties of powdered samples of the four members of the $[Ln^{III}(W_5O_{18})_2]^{9-}$ family (Ln = Tb^{3+}, Dy^{3+}, Ho^{3+}, and Er^{3+}) in the form of the $\chi_m T$ product versus T are shown in Figure 7. At room temperature, all samples show $\chi_m T$ values close to those expected for the free trivalent ion: $\chi_m T = 11.92$ emu K^{-1} mol^{-1} for Tb^{3+} ($J = 6$, $g = {}^3/_2$, $\chi_m T_{\text{free ion}} = 11.81$), 13.31 emu K^{-1} mol^{-1} for Dy^{3+} ($J = {}^{15}/_2$, $g = {}^4/_3$, $\chi_m T_{\text{free ion}} = 14.17$), 14.05 emu K^{-1} mol^{-1} for Ho^{3+} ($J = 8$, $g = {}^5/_4$, $\chi_m T_{\text{free ion}} = 14.06$), and 10.85 emu K^{-1} mol^{-1} for Er^{3+} ($J = {}^{15}/_2$, $g = {}^6/_5$, $\chi_m T_{\text{free ion}} = 11.475$). When the temperature decreases, the $\chi_m T$ value gradually decreases because of depopulation of the highest crystal-field levels.

Figure 8 shows the $\chi_m T$ versus T plots for the six members of the $[Ln(\beta_2\text{-}SiW_{11}O_{39})]^{13-}$ family (Ln = Tb^{3+}, Dy^{3+}, Ho^{3+}, Er^{3+}, Tm^{3+}, and Yb^{3+}). Again, at room temperature, the $\chi_m T$ values are close to free ion values: $\chi_m T = 11.16$ emu K^{-1} mol^{-1} for Tb^{3+}, 13.71 emu K^{-1} mol^{-1} for Dy^{3+}, 14.21 emu K^{-1} mol^{-1} for Ho^{3+}, 11.56 emu K^{-1} mol^{-1} for Er^{3+}, and 6.82 emu K^{-1} mol^{-1} for Tm^{3+} ($J = 6$, $g = {}^7/_6$, $\chi_m T_{\text{free ion}} = 7.15$), 2.68 emu K^{-1} mol^{-1} for Yb^{3+} ($J = {}^7/_2$, $g = {}^8/_7$, $\chi_m T_{\text{free ion}} = 2.57$).

Determination of LF Parameters. The LF describes the effect of the electric field due to the surrounding ligands acting on a given paramagnetic metal ion. For the C_4 point group, the
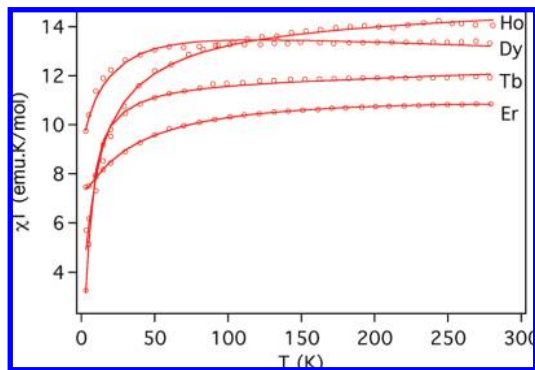
Figure 7. Plots of the $\chi_m T$ product versus T for the four members of the $Na_9[Ln(W_5O_{18})_2]\cdot xH_2O$ family (Ln = Tb, Dy, Ho, and Er). Solid lines are the best simultaneous fits obtained using the Hamiltonian in eq 2 and the conditions in eq 3.

LF Hamiltonian can be written taking into account the operator equivalent as

$$\hat{H} = A_2^0r^2\alpha\hat{O}_2^0 + A_4^0r_4\beta\hat{O}_4^0 + A_4^4r^4\beta\hat{O}_4^4 + A_6^0r^6\gamma\hat{O}_6^0 + A_6^4r^6\gamma\hat{O}_6^4 \quad (1)$$

where α, β, and γ coefficients are the constants tabulated by Stevens for each lanthanide,[20] $\hat{O}_k^q$ are the operator equivalents and can be expressed as polynomials of the total angular momentum operators,[21] r^k are radial factors, and A_k^q are numerical parameters. The products A_k^q r^k are the parameters to be determined.

In the $[Ln^{III}(W_5O_{18})_2]^{9-}$ family, each anionic $[W_5O_{18}]^{6-}$ moiety is twisted 44.2° with respect to the other. This skew angle is very close to that expected for an ideal D_{4d} symmetry ($\phi = 45°$). Hence, an idealized D_{4d} symmetry can be assumed in this case. For this symmetry, the two LF terms with $q \neq 0$ ($A_4^4r^4$ and $A_6^4r^6$) vanish, and the LF Hamiltonian can be simplified to give

$$\hat{H} = A_2^0r^2\alpha O_2^0 + A_4^0r^4\beta O_4^0 + A_6^0r^6\gamma O_6^0 \quad (2)$$

In the $[Ln(\beta_2\text{-}SiW_{11}O_{39})]^{13-}$ family, this assumption may still be valid and, even if the distortions in the square antiprism are larger, the two LF terms with $q \neq 0$ are expected to be small and can be neglected. Ishikawa demonstrated that the LF parameters of an isomorphic series of lanthanide com-
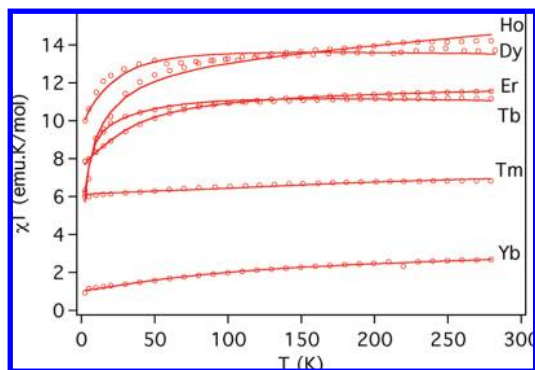

Figure 8. Plots of the $\chi_m T$ product versus T for the six members of the $K_{13}[Ln(\beta_2\text{-}SiW_{11}O_{39})_2]\cdot xH_2O$ family (Ln = Tb, Dy, Ho, Er, Tm, and Yb). Solid lines are the best simultaneous fits obtained using the Hamiltonian in eq 2 and the conditions in eq 3.

Table 5. LF Parameters Determined for the $[LnW_{10}]^{9-}$ and $[LnW_{22}]^{13-}$ Families (in cm^{-1})

Ln	$[LnW_{10}]^{9-}$ series			$[LnW_{22}]^{13-}$ series		
	$A_2^0r^2$	$A_4^0r^4$	$A_6^0r^6$	$A_2^0r^2$	$A_4^0r^4$	$A_6^0r^6$
Tb	−36.8	−89.0	−5.2	−11.3	−137.4	−7.1
Dy	−153.6	−145.5	16.3	−88.3	−134.4	7.0
Ho	−270.4	−202.0	37.7	−165.2	−131.3	21.1
Er	−387.2	−258.5	59.2	−242.2	−128.2	35.2
Tm				−319.2	−125.2	49.2
Yb				−396.1	−122.1	63.3

plexes could be determined by a simultaneous fit of all of the $\chi_m T$ values under the assumption that the LF parameters from the f^8 system to the f^{13} system show a linear variation.[6] Under these conditions, the $A_k^q r^k$ coefficients can be expressed as a linear function of the number of f electrons, n_f:

$$A_k^q r^k = a_k^q + b_k^q(n_f - 10.5) \quad (3)$$

where n_f values range from 8 to 13 when moving from Tb^{3+} to Yb^{3+}. The constant 10.5 represents the average value of n_f for the full series.

Following the Ishikawa procedure, we have estimated the best set of LF parameters in both families of rare-earth POMs (Figure 6 and Table 5). These values are extracted from a simultaneous fit of 40 $\chi_m T$ values per compound from 2 K up to room temperature. Figures 7 and 8 show the excellent agreement between the experimental values and the theoretical expectations. If we compare these two sets of LF parameters with those derived from the phthalocyaninatolanthanide complexes (Figure 6), the most important difference is the sign of the $A_0^2r^2$ parameter, which is negative in the two rare-earth POM families but positive in the phthalocyaninatolanthanide family (see Table 5). We can associate this change in the sign with differences in the axial distortion of the coordination site. In fact, while the POM derivatives exhibit an axial compression, axial elongation of the square antiprism is observed in the phthalocyaninatolanthanide complexes. This different sign has important consequences in the structure of the low-lying energy levels and in the dynamic magnetic properties of these complexes, as we will discuss in the next sections.

A simultaneous fit of the susceptibility data and ^{17}O and ^{183}W NMR paramagnetic shifts has been performed for the $[Ln^{III}(W_5O_{18})_2]^{9-}$ family. The room temperature ^{17}O and ^{183}W NMR chemical shifts have been extracted from different works.[22] This simultaneous fit does not have a good and unique solution, and the result depends on how the weight of each experimental>property data is treated. NMR fit gives a solution with positive values of $A_0^2r^2$, whereas the opposite is obtained from the susceptibility fit. These differences may come from different causes. First, the NMR experiments are performed in solution, whereas susceptibility measurements are performed on powdered samples. In solution, even if the general configuration of the complex is unchanged, changes in the bond lengths and angles can occur. On the other hand, in POMs, an important electron delocalization from the paramagnetic center to oxygen and wolfram

atoms has been proven, and important contact contributions to the chemical shift can be possible even for apical atoms. For this reason we have decided not to use the NMR data but more reliable techniques such as electron paramagnetic resonance (EPR) and specific heat.

Electronic Structure of $[Ln(W_5O_{18})_2]^{9-}$ and $[Ln(\beta_2\text{-}SiW_{11}O_{39})_2]^{13-}$. The electronic structure of the ground-state multiplet of each lanthanide complex expressed in terms of the LF parameters can be obtained from a diagonalization of the $(2J + 1)$-dimension eigenmatrix. Figure 9 shows the $2J + 1$ energy sublevels of the ground state of each system as a function of the M_J values.

a. $[Tb(W_5O_{18})_2]^{9-}$ (1) and $[Tb(\beta_2\text{-}SiW_{11}O_{39})_2]^{13-}$ (5) Systems. In both systems, the ground substate is that with the lowest M_J value, 0. In the case of the Lindqvist derivative, the first excited level, $M_J = \pm 1$, is around 15 cm^{-1} above the singlet ground substate, while in the Keggin derivative, the $M_J = \pm 1$ doublet is almost degenerate with the ground substate. The structure of the energy level pattern is very similar in both systems. For the low $|M_J|$ values, one can observe the distribution of levels expected for a positive axial zero-field splitting (ZFS) of order 2, $A_2^0 r^2 \alpha > 0$. The highest $|M_J|$ value, ± 6, is stabilized because of the negative axial ZFS of order 4, $A_4^0 r^4 \beta < 0$, and the doublet $M_J = \pm 6$ can become the ground substate for big values of the $A_2^0 r^2 / A_4^0 r^4$ ratio. In fact, for **5**, this ratio is large enough to place the levels $M_J = 0$ and ± 6 very close in energy. In the Ishikawa complex, the $M_J = \pm 6$ doublet is even more stabilized and becomes the ground substate because of the fact that $A_2^0 r^2 \alpha < 0$.

b. $[Dy(W_5O_{18})_2]^{9-}$ (2) and $[Dy(\beta_2\text{-}SiW_{11}O_{39})_2]^{13-}$ (6) Systems. The lowest Kramers doublet for both systems corresponds to $M_J = \pm^{11}/_2$. The first excited doublet $M_J = \pm^9/_2$ is very close in energy to the ground substate in both systems (with gaps of ca. 4 and 2 cm^{-1}, respectively).

c. $[Ho(W_5O_{18})_2]^{9-}$ (3) and $[Ho(\beta_2\text{-}SiW_{11}O_{39})_2]^{13-}$ (7) Systems. For the Ho^{3+} complexes, the ground substate is the doublet $|M_J| = \pm 4$, and the first excited level is the doublet $M_J = \pm 5$ with energy gaps of 16 and 6 cm^{-1}, respectively.

d. $[Er(W_5O_{18})_2]^{9-}$ (4) and $[Er(\beta_2\text{-}SiW_{11}O_{39})_2]^{13-}$ (8) Systems. The ground substate is the $M_J = \pm^{13}/_2$ doublet in both systems. For **4**, the $M_J = \pm^1/_2$ doublet is very close in energy, around 3 cm^{-1}, and the $M_J = \pm^{15}/_2$ doublet is at 17 cm^{-1}. In **8**, the ground substate is more stabilized and the doublets with $M_J = \pm^1/_2$ and $\pm^{15}/_2$ are at 24 and 33 cm^{-1}, respectively. These three doublets are well isolated from the rest of the doublets. This scheme results from an opposite effect of the different LF terms. High $|M_J|$ values are the usually stabilized by a negative second-order LF term $(A_2^0 r^2 \alpha)$, but in this case, the higher order LF terms stabilize the $M_J = \pm^1/_2$ doublet. Notice that this energy level scheme is completely different from that reported for the Ishikawa

complex. In fact, in this complex, the $M_J = \pm^1/_2$ doublet becomes the ground substate because it is strongly stabilized as a result of a positive second-order LF term.

e. $[Tm(\beta_2\text{-}SiW_{11}O_{39})_2]^{13-}$ (9) System. The ground substate for this complex is the doublet with the highest $|M_J|$ value ($=\pm 6$). The energy gap between this doublet and the first excited doublet, $M_J = \pm 3$, is around 400 cm^{-1}. This large energy gap makes the ground substate the most populated level even at room temperature with a population ratio of 80%. The constant value of $\chi_m T$ in all ranges of temperature is due to this small depopulation of the other LF sublevels.

f. $[Yb(\beta_2\text{-}SiW_{11}O_{39})_2]^{13-}$ (10) System. In this complex, the ground substate is the doublet with $M_J = \pm^5/_2$, with the first excited sublevel ($M_J = \pm^7/_2$) placed at 100 cm^{-1}. The energy pattern is the result of a high and negative second-order LF term, which stabilizes the $M_J = \pm^7/_2$ doublet, and positive fourth- and sixth-order LF terms, which stabilize the $M_J = \pm^5/_2$.

Low-Lying Energy Levels in 4. Using the indirect information provided by the study of the thermal dependence of the magnetic susceptibility, the LF parameters and the resulting energy splittings of the ground-state multiplets of the 10 POM lanthanide complexes have been estimated. This method has been employed to determine the ground substates of these complexes. However, the resulting splitting structures contain one or various excited sublevels that are very close in energy, or even degenerate, to the ground sublevel. In these conditions, the energy splitting of these low-lying energy levels can only be considered approximate, and other techniques are required to obtain more quantitative information. Let us illustrate this point with the $[Er(W_5O_{18})_2]^{9-}$ derivative (**4**), which shows a complex splitting structure of the low-lying levels, with three levels separated by less that 20 cm^{-1}. As complementary techniques, we have used EPR and specific heat.

The powder X-band EPR spectrum of the sodium salt of **4**, performed at low temperatures, shows a strong signal around 800 G (Figure 10). The intensity of this signal increases when the temperature increases from 8 to 25 K. This indicates that the transition associated with this signal has its origin in an excited state. Taking into account the energy levels obtained for **4** with an ideal D_{4d}-symmetry LF Hamiltonian, only the transition within the excited doublet $M_J = \pm^1/_2$ is allowed. Evaluation of the energy levels, including Zeeman interaction for different orientations of the external magnetic field, places this transition within the experimental range of magnetic fields available in the X band. The temperature dependence of the intensity of this signal can be reproduced by assuming a three-level energy pattern, as derived from the susceptibility analysis. In this model, the doublet $\pm^1/_2$ is an excited state that has to be situated 17.5 cm^{-1} above the ground doublet $\pm^{13}/_2$ and 11.1 cm^{-1} below the next excited doublet $\pm^{15}/_2$. The powder EPR spectra for the other members of the family have also been

(31) Ozeki, T.; Yamase, T. *Acta Crystallogr.* **1993**, *C49*, 1577.
(32) Ozeki, T.; Yamase, T.; Ueda, K. *Acta Crystallogr.* **1993**, *C49*, 1572.
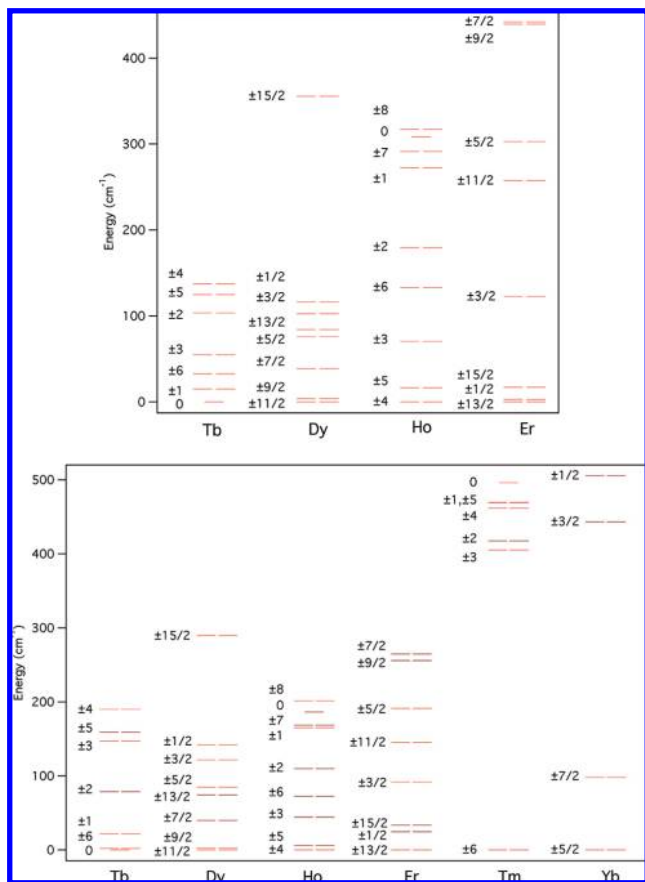(33) Sawada, K.; Yamase, T. *Acta Crystallogr.* **2002**, *C58*, 149.

Figure 9. Energy level diagrams of the ground-state multiplets for $Na_9[Ln(W_5O_{18})_2] \cdot xH_2O$ and $K_{13}[Ln(\beta_2\text{-}SiW_{11}O_{39})_2] \cdot xH_2O$ families derived from the susceptibility data.
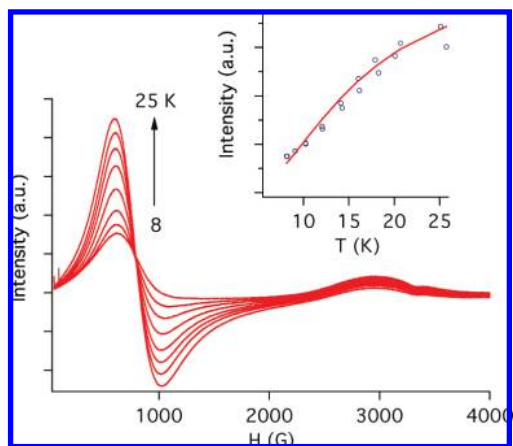

Figure 10. X-band EPR spectra for complex **4** at different temperatures from 8 to 25 K. Inset: Evolution of the intensity of the signal as a function of the temperature. The solid line is the theoretical intensity for a three-level model (see the text for further discussion).

performed, but the very complex structure observed has prevented us from extracting useful information on the low-lying energy spectrum.

Specific heat measurements support that the energy gap between the ground doublet and the first excited one is not smaller than ca. 17 cm^{-1} in **4**, in full agreement with the EPR data. The measurements, performed down to 0.35 K and under zero magnetic field, are shown in Figure 11. They are compared with data measured, under identical conditions,
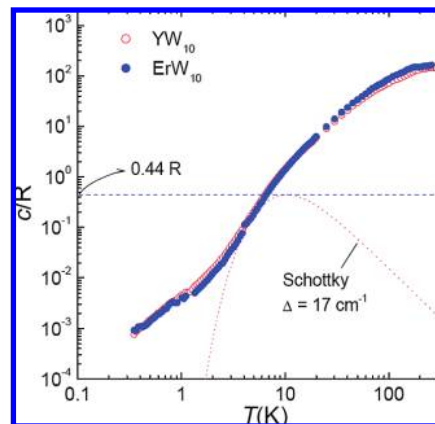

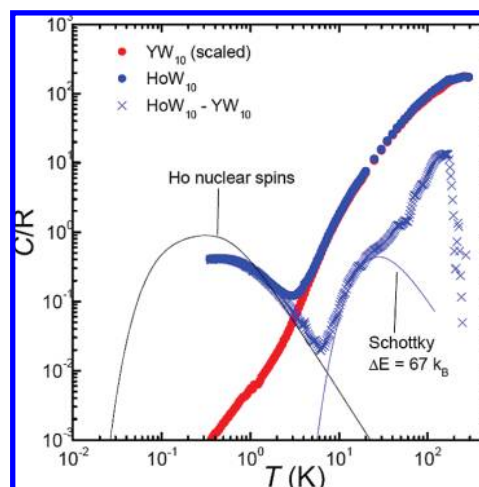**Figure 11.** Specific heat of **4** at zero field. Thin lines show the different contributions.

Figure 12. Specific heat of **3** at zero field compared with the data measured on the $[Y(W_5O_{18})_2]^9$ nonmagnetic compound.

on the nonmagnetic derivative containing $[Y(W_5O_{18})_2]^{9-}$. We observe that the two sets of data overlap, within the experimental uncertainties, over the whole temperature range. This is a clear indication that the specific heat is fully dominated by contributions that are equally present in the two compounds. These arise from (a) vibrations of the lattice (acoustic and optical phonons), which dominate above 2 K, and (b) the hyperfine split levels of ^{183}W (14.3% in natural W) nuclear spins ($I = \frac{1}{2}$). In the temperature range between 2 and 8 K, the specific heat is approximately proportional to T,[3] in agreement with the Debye model for the specific heat of acoustic phonons. The fit gives a Debye temperature $\Theta_D = 57(2)$ K. Concerning the electronic levels of the erbium ions, we can estimate from these data a lower bound for the energy difference between the ground state and the first excited doublet. For two doublets separated an energy of Δ, the Schottky shows a peak at a temperature $T_{max} = 0.42\Delta/k_B$, where $c_{max} = 0.44R$. Because no such contribution is observed below 10 K, the gap Δ should not be smaller than 17 cm^{-1}. An illustrative example of this magnetic contribution is provided by the dotted line in Figure 11.

Specific heat measurements have also been performed on **3** (Figure 12). As described above for **4**, we have included the data measured on the nonmagnetic $[Y(W_5O_{18})_2]^{9-}$ compound as a reference. In this case, though, we have
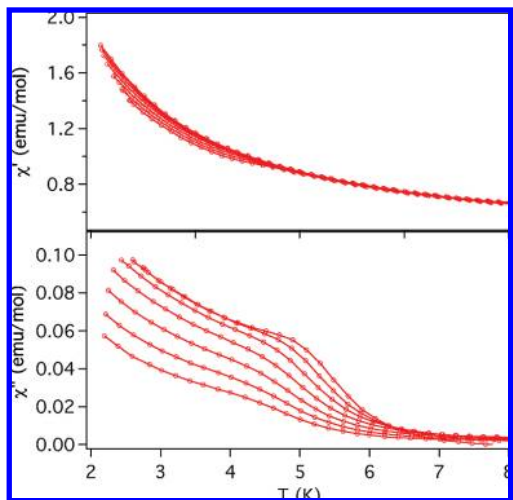
Figure 13. In-phase and out-of-phase dynamic susceptibility of **3**. High-frequency measurements from left to right: 1000, 1500, 2200, 3200, 4600, 6800, and 10000 Hz.

rescaled the latter data by a factor 1.2 to make them overlap with the data obtained for $[Ho(W_5O_{18})_2]^9$ above 250 K (where only lattice vibrations contribute). This factor might arise from the effect that the molecular mass has on the energies of the vibration modes or from a small error in the determination of the sample's mass. As observed for **4**, lattice vibrations dominate above 5 K. Yet, there is a small difference between the curves measured on the two compounds (blue crosses in Figure 12), which might be compatible with the presence of a Schottky anomaly centered near 25 K. This would correspond to an energy-level splitting on the order of 67 k_B. The additional contribution observed at even higher temperatures is probably an artifact related to the large contribution introduced by the apiezon grease. Therefore, what we see might be caused by a nonperfect subtraction of the addenda. The curves measured on the magnetic and nonmagnetic compounds deviate below 4 K. This contribution suggests the presence of low energy levels (energy splitting on the order of 1 k_B), which probably arise from the hyperfine split levels of the holmium nuclear spins (see the prediction in Figure 12). Therefore, and in contrast with the situation observed in the case of erbium nuclei, the holmium nuclear spins remain in thermal equilibrium down to very low temperatures. The different behavior of the nuclear specific heat might be associated with the different spin–lattice relaxation times (or spin-tunneling times) measured for the electronic magnetic moments of erbium and holmium: $\tau \approx 10^{-3}$ s and $\tau \approx 10^{-4}$ s, respectively.

ac Magnetic Susceptibility Measurements. Dynamic magnetic susceptibility measurements have been performed at low temperatures (down to 2 K) for the 10 salts of the two series of POM complexes.

In the $[Ln(W_5O_{18})_2]^{9-}$ series, only Ho (**3**) and Er (**4**) derivatives exhibit clear frequency-dependent out-of-phase signals (χ'') at low temperatures. Thus, upon cooling, a maximum or a shoulder is observed at high frequency (1000–10000 Hz), followed by sharp increases in χ'' at lower temperatures (Figures 13 and 14). In turn, the Dy derivative (**2**) only shows an increase in χ'' below 4 K (SI 5 in the
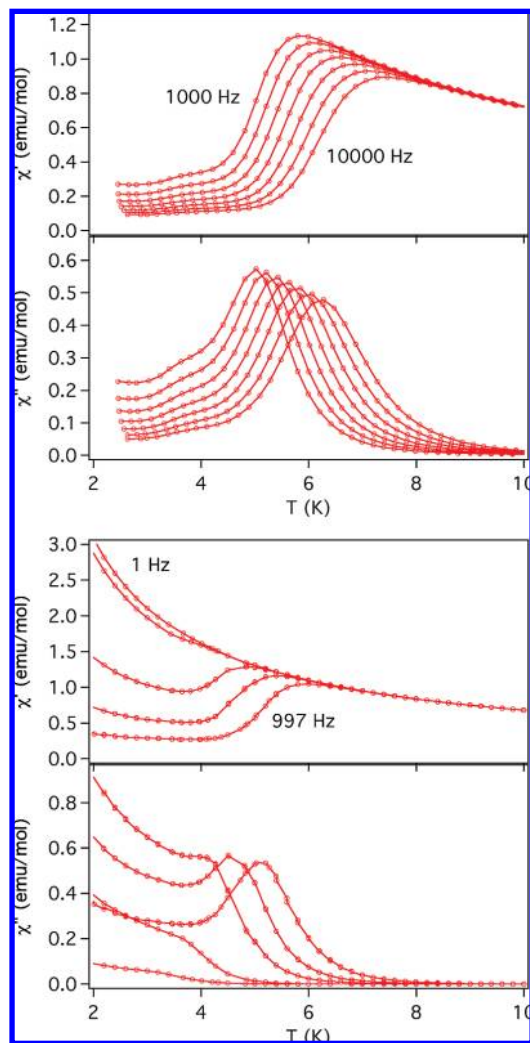

Figure 14. In-phase and out-of-phase dynamic susceptibility of **4**. (Top) High-frequency measurements from left to right: 1000, 1500, 2200, 3200, 4600, 6800, and 10000 Hz. (Bottom) Low-frequency measurements from top to bottom: 1, 10, 110, 332, and 997 Hz.

Supporting Information), while Tb (**1**) does not show any χ'' signal down to 2 K (SI 4 in the Supporting Information). In the $[Ln(\beta_2\text{-}SiW_{11}O_{39})_2]^{13-}$ series, Er (**8**) and Yb (**10**) derivatives show a shoulder at high frequencies and a divergence in χ'' at lower temperatures (Figure 5 and SI 10 in the Supporting Information). In turn, Dy (**6**) and Ho (**7**) derivatives only show an increase in χ'' below 6 K (SI 7 and SI 8 in the Supporting Information), while Tb (**5**) and Tm (**9**) do not show any χ'' signal down to 2 K (SI 5 and SI 9 in the Supporting Information).

$[Ho(W_5O_{18})_2]^{9-}$. In compound **3**, one observes a shoulder in χ'' situated at ca. 5 K (for a frequency of 10 000 Hz), which is strongly frequency-dependent and tends to disappear when the frequency is reduced, and a divergence at lower temperatures (Figure 13). This behavior closely resembles that of the Er derivative (**4**) when studied at low frequencies.

$[Er(W_5O_{18})_2]^{9-}$. The magnetic properties of **4** reveal the typical features associated with the SMM behavior. Thus, both χ' and χ'' show strong frequency dependencies, which indicate the presence of a slow relaxation process involving
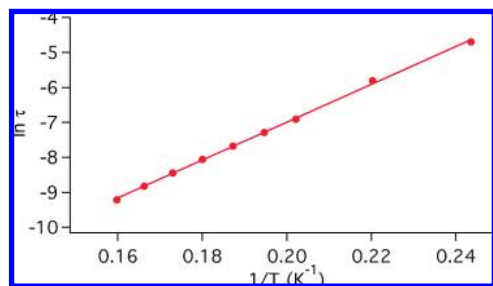
Figure 15. Relaxation-time fitting to the Arrhenius law in the 110−10000 Hz interval for **4**.

an energy barrier for the reversal of the magnetization. Depending on the frequency of the applied ac field, χ' presents a maximum between 5.5 and 7.5 K, while χ'' has also a maximum between 5 and 6.2 K for 1000 and 10 000 Hz, respectively (Figure 14). Below the blocking temperature, the susceptibility increases as the system is cooled down and this increase becomes more pronounced as the frequency is decreased. In this situation, the maximum, which shifts toward lower temperatures when the frequency is decreased, becomes closer to the divergence, appearing only as a shoulder. The divergence may be indicative of a fast relaxation process within the ground-state doublet $M_J = \pm^{13}/_2$ because it is the only populated at these temperatures according to the EPR and specific heat data (Figures 10 and 11).

Analyses of the frequency dependence of the χ'' peaks through an Arrhenius plot permits the estimation of the magnetization−relaxation parameters in this system (Figure 15). Best fitting affords a barrier height (U_{eff}/k_B) of 55.2 K with a preexponential factor (τ_O) of 1.6×10^{-8} s. Given the good insulation of Er^{3+} ions provided by the diamagnetic polyoxowolframate framework (the shortest Er−Er distance in the crystal structure is 11.225 Å), the slow relaxation process exhibited by **4** should be considered as a single-molecule property.

To discard the presence of magnetic impurities that might be responsible for the "anomalous" increase of the magnetic susceptibility below the blocking temperature, the frequency dependence of the ac susceptibility of **4** was measured at different temperatures (Figure 16). The fitting of the experimental data to a Cole−Cole function suggests the presence of a very narrow distribution of relaxation times (least-squares fittings yielded $\alpha = 0.82$). Besides, no additional out-of-phase peaks are observed, indicating that at any temperature there is only one dominating relaxation process related to a single magnetic species.

To understand the apparently "strange" behavior of the dynamic susceptibility, we must bring into play the definition of the Cole−Cole function.[23] According to it, χ'' can be defined as

$$\chi'' = (\chi_T - \chi_S)\frac{(\omega\tau)^{\alpha}\sin(\alpha\pi/2)}{1 + (\omega\tau)^{2\alpha}} \quad (4)$$

This expression simplifies to the well-known Debye equation when $\alpha = 1$. The χ_T and χ_S susceptibilities stand for the equilibrium and high-frequency (or adiabatic) limits, respectively. When measured as a function of the frequency, these
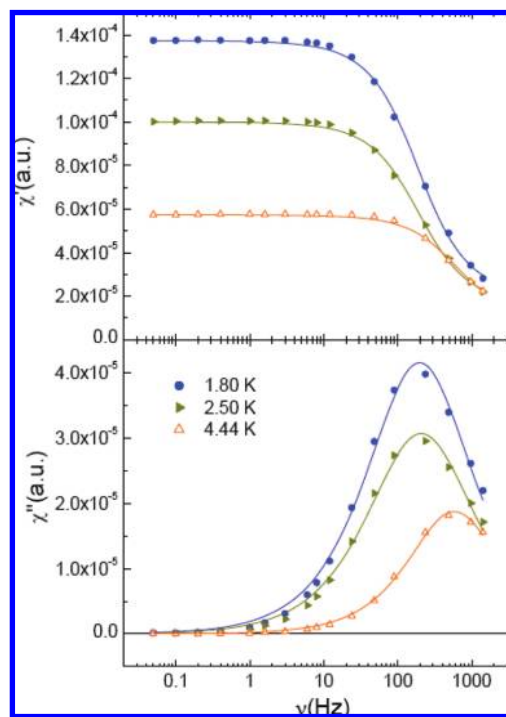

Figure 16. ac susceptibility of **4** measured as a function of the frequency at the temperatures indicated by the caption. Top: Real component. Bottom: Imaginary component. Solid lines represent the best fitting of the experimental data to a Cole−Cole function, yielding $\alpha = 0.82$.

two parameters remain constant and a maximum of χ'' is observed when the τ product is equal to 1, exactly as is experimentally observed in this case. On the other hand, things are quite different when χ'' is measured as a function of the temperature. Then, not only τ but also χ_T (and to a much lesser extent χ_S) depend on the temperature. Usually (e.g., in the case of Mn12 and many other SMMs), these parameters remain almost constant because the relaxation time depends exponentially on the temperature in the temperature range accessible to ac susceptibility experiments. On the contrary, in this particular case, the relaxation time tends to become independent of the temperature below approximately 3 K. This can be seen from the fact that the maxima of χ'' do not shift to lower frequencies as T decreases. In other words, there is a crossover from a thermally activated relaxation mechanism, above 3 K, to a direct (or pure tunneling) mechanism below 3 K. This temperature-independent tunneling mechanism is very fast compared to what is usually observed in other SMMs: from the Cole−Cole fits, we infer relaxation times on the order of milliseconds. Still, at any temperature, one or the other is dominating (i.e., provides the fastest relaxation channel). Therefore, when we measure χ'' as a function of the temperature at fixed frequency, the susceptibility does not get fully blocked because the relaxation time remains very small and it does not change with decreasing T. As a result, and according to the Cole−Cole equation, the imaginary component "inherits" the variation with temperature of the equilibrium susceptibility, which is approximately proportional to the reciprocal temperature. The ratio of χ'' to the equilibrium susceptibility depends on the frequency, and for this reason, χ'' still depends on the frequency.
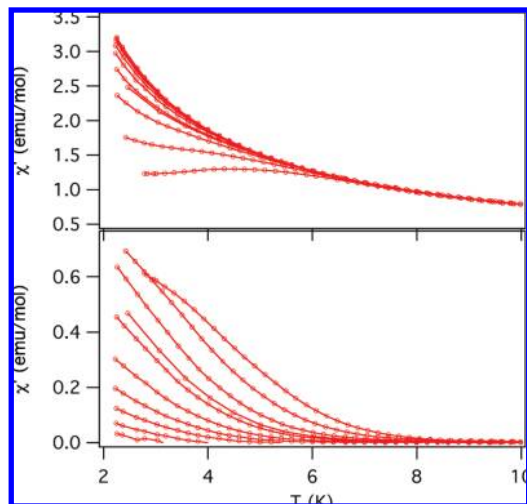
Figure 17. In-phase (top) and out-of-phase (bottom) dynamic susceptibility of **8**. High-frequency measurements from left to right: 1000, 1500, 2200, 3200, 4600, 6800, and 10 000 Hz.

In summary, the observed temperature dependence of χ'' reflects the existence of a fast tunneling relaxation channel. This relaxation mechanism becomes dominant over thermally activated processes already below approximately 3 K. In this particular case, it is so fast that the superparamagnetic blocking (i.e., the condition $\tau \gg 1$) is only attained for very high frequencies and prevents χ'' from vanishing completely.

The two relaxation processes, which are clearly seen in **4**, are still present in **3**. The main difference is that the tunneling process dominates the low-temperature behavior and, therefore, the thermally activated relaxation process can only be observed for the higher frequencies.

[Dy(β_2-SiW$_{11}$O$_{39}$)$_2$]$^{13-}$. Compound **6** exhibits a strong frequency dependence of the out-of-phase signal below 10 K (SI 6 in the Supporting Information). Nevertheless, no blocking is observed down to 2 K, preventing extraction of the dynamical parameters.

[Ho(β_2-SiW$_{11}$O$_{39}$)$_2$]$^{13-}$. In compound **7**, χ'' increases continuously below 6 K without showing any blocking down to 2 K (SI 7 in the Supporting Information). As previously observed in the Er derivative of the Keggin series (**8**) and in the Ho derivative of the Keggin series (**7**), the slow relaxation process characteristic of the SMM behavior is faster than that in the Lindqvist Ho analogue (**3**) and therefore lower temperatures are needed to fully characterize **7**.

[Er(β_2-SiW$_{11}$O$_{39}$)$_2$]$^{13-}$. The ac susceptibility curves of **8** are shown in Figure 17. In this derivative, strong frequency dependencies in χ'' and χ' are also observed, which are indicative of a SMM behavior. However, the maxima in the χ'' peak are not observed even at 2 K, indicating that the magnetization relaxes much faster in this compound than in **4**. Thus, in **8**, the blocking temperature has to be situated below this temperature. Lower temperatures are now required to complete the characterization of this molecular nanomagnet.

[Yb(β_2-SiW$_{11}$O$_{39}$)$_2$]$^{13-}$. A strong frequency dependence of the out-of-phase signal of **10** below 10 K is also observed (SI 9 in the Supporting Information). As commented on above, additional lower temperature magnetic characteriza-

tion is required to extract information concerning the dynamical parameters.

Final Discussion. In the last years, POM chemistry has motivated an increasing interest in molecular magnetism by providing ideal examples to study the exchange interactions and the electron hopping in high-nuclearity magnetic and mixed-valence clusters.[24] Very recently, new possibilities in the emerging area of quantum computing have been foreseen for these magnetic complexes.[25] In a recent communication, we have shown that POM complexes containing a single lanthanide ion can provide examples of SMMs.[8] Almost simultaneously, the first example of a polynuclear magnetic cluster assembled by POMs exhibiting SMM behavior has also been reported.[26] These novel properties of POMs enhance the relevance of these inorganic molecules in molecular magnetism because a plethora of a new series of SMMs can be foreseen by a suitable choice of POM ligands.

We have shown in this work that POM complexes containing a single lanthanide ion in an antiprismatic geometry with approximately D_{4d} symmetry can exhibit SMM behavior. This has been demonstrated in the families [Ln(W$_5$O$_{18}$)$_2$]$^{9-}$ (Ln^{III} = Tb, Dy, Ho, and Er) and [Ln(β_2-SiW$_{11}$O$_{39}$)$_2$]$^{13-}$ (Ln^{III} = Tb, Dy, Ho, Er, Tm, and Yb). Magnetic relaxation properties typical of SMMs have been observed in various members of the two families, namely, the Ho and Er derivatives of the former series (compounds **3** and **4**) and the Dy, Ho, Er, and Yb derivatives of the second series (compounds **6**−**8** and **10**). In the [Er(W$_5$O$_{18}$)$_2$]$^{9-}$ derivative (**4**), the presence of a frequency-dependent maximum in χ'' has enabled us to estimate the energy barrier for the reversal of the magnetization (U_{eff} = 55.2 K). Although the other members also show frequency-dependent χ'' signals, this energy barrier seems to be smaller and thus the blocking temperatures are expected to be situated below 2 K.

To understand why these six compounds exhibit this behavior, we have estimated the LF parameters for all of the reported complexes and the resulting splitting of the J ground-state multiplet of the lanthanide ion. We can observe that these compounds have ground-state doublets with large $|M_J|$ values, thus achieving an easy axis of the magnetization (in the Dy derivatives with $J = {}^{15}/_2$, $M_J = \pm^{11}/_2$ is the ground state; in the Ho derivatives with $J = 8$, $M_J = \pm 4$ is the ground state; in the Er derivatives with $J = {}^{15}/_2$, $M_J = \pm^{13}/_2$ is the ground state; in the Yb derivative with $J = {}^{7}/_2$, $M_J = \pm^5/_2$ is the ground state). With these LF parameters, the ground state of the Tb derivatives (**1** and **5**) turns out to be a singlet $M_J = 0$. This explains why these last two compounds do not behave as SMMs.

If we compare these POM lanthanide derivatives with the phthalocyaninatolanthanide complexes reported by Ishikawa et al.,[7] one can find significant differences and similarities in the magnetic relaxation properties:

Thus, while in POM complexes, the Er derivatives behave as SMMs, in the phthalocyaninato complexes, they do not show any sign of SMM behavior. In turn, the Tb derivative behaves as a SMM in the phthalocyaninato complexes but not in the POMs. These differences come from the different LF splittings as a consequence of the different structural

distortions observed in the lanthanide site. Thus, while POM complexes show an axial compression of the lanthanide coordination site, in the phthalocyaninato family, an axial elongation is observed. This small structural change leads to different LF parameters and, in particular, to a change of the sign of the axial ZFS parameter of order 2, $A_2^0 r^2$. As a consequence, the lowest-lying energy levels for erbium and terbium are very different and almost reversed in the two classes of complexes. In fact, while in the case of erbium the POM ligands stabilize larger $|M_J|$ values, the phthalocyaninato ligand stabilizes the lowest value, $M_J = \pm^1/_2$. In a similar way, in the terbium case, the POM derivatives stabilize the singlet $M_J = 0$, while the doublet with the largest J value, $M_J = \pm 6$, becomes the ground state in the phthalocyaninato derivative.

On the other hand, one can notice that the magnetic relaxation processes are faster in POMs than in the phthalocyaninato complexes showing SMM behavior. The reason can be related with the smaller separation between the lower-lying energy levels caused by the LF splitting, which in POM derivatives often contain two or more levels separated by less than 30 cm^{-1}. Another related question is the observation that, in general, for a given lanthanide, the magnetization of the Keggin-type series relaxes faster than that for the Lindqvist one. One observes in Figure 9 that in both series the LF leads to a similar pattern for the lower-lying energy levels. Therefore, similar magnetic relaxation properties should be expected. However, the sublevel structures have been determined under the assumption of a purely axial D_{4d} symmetry, when nonaxial distortions are clearly present in the Keggin-type derivatives (the two coordinating planes are not parallel). This type of distortion, which is absent in the Lindqvist-type derivatives, may account for the faster magnetic relaxation observed in the Keggin-type derivatives. In fact, apart from having a non-negligible influence on the sublevel structures, this distortion can also mix the different wave functions.

A final point that deserves to be discussed concerns the divergence in χ'' observed in this class of mononuclear lanthanide SMMs at temperatures below the blocking temperature. Such a behavior is specific for this class of SMMs and is in sharp contrast to that observed in the cluster-based SMMs (Mn$_{12}$, for example) in which χ'' tends to vanish below the blocking temperature. In the mononuclear lanthanide SMMs, both processes, the thermally activatd

relaxation process giving rise to the observation of a maximum in χ'' due to the superparamagnetic blocking of the magnetic moments and a very fast tunneling process giving rise to a divergence in χ'', seem to coexist. This is clearly observed in **4** but also appears in other derivatives, such as, for example, in **3** and **10**, although in these compounds, the maximum in χ'' is less pronounced and is often masked by the divergence. Notice that this kind of behavior was already observed in the phthalocyaninatolanthanide complexes. In that case, the divergence was attributed to the presence of intermolecular magnetic interactions between adjacent complexes. However, in our case, the large intermolecular distances provided by the bulky POM clusters keep the lanthanides well-insulated (the shortest Er−Er distance in **4** is 11.225 Å) and only the magnetic dipolar interactions are possible. In these conditions, the divergence seems to be rather associated with a single-molecule property. A preliminary investigation on the low-temperature spin dynamics of these systems suggests that this divergence corresponds to a very fast quantum tunneling process within the $\pm M_J$ ground-state doublet. Moreover, this anomalous behavior appears as the most attractive feature of these materials because for the first time it enables the direct study of the crossover between thermally activated relaxation and direct tunneling by means of a single, and simple, experimental technique: linear ac susceptibility.

Supporting Information Available: Crystal structure files in CIF format (files 1 and 2 correspond to compounds **8** and **9**, respectively), FT-IR spectrum and EPMA data for the whole set of compounds together with the ac magnetic susceptibility data for **1**, **2**, **5**−**7**, **9**, and **10**. This material is available free of charge via the Internet at http://pubs.acs.org.

IC801630Z